nature communications

Article | Article in Press

https://doi.org/10.1038/s41467-026-79377-w

Mitigating brittleness in ceramics via transformation- and twinning-induced plasticity

Received: 1 February 2026

Accepted: 13 October 2026

Published online: 19 November 2026

Check for updates

Yong Huang[1], Zhuo Chen[1], Kiana Rostamipour[2], Rainer Hahn[3], Verena Maier-Kiener[4], Jozef Keckes[4], Christian Mitterer[4], Nikola Koutná[2] & Zaoli Zhang[1]

Ceramics usually exhibit inherent brittleness at room temperature due to their strong covalent/ionic bonding and few active slip systems. Consequently, ceramics exhibit a low damage-bearing capacity and typically sudden failure prior to yielding. Thus, achieving room-temperature plasticity while maintaining or enhancing the strength of ceramics remains critical and challenging. Here, we report a promising strategy to address this problem by concurrently activating twinning-induced plasticity and transformation-induced plasticity in a monolithic TaN ceramic film. Through precisely controlled physical vapor deposition, we stabilize the metastable δ-TaN phase with hierarchical nanotwinned architectures. Then, by combining micromechanical tests, atomic-resolution characterization, and ab initio molecular dynamics simulations, we demonstrate that the synergy of phase transformation and twinning brings exceptional damage tolerance and plasticity, achieving up to 60% compressive strain without catastrophic fracture alongside a hardness of ~43 GPa. Our work not only proves the feasibility of twinning and transformation-induced plasticity synergy in designing ultrahard and ductile materials, but also highlights the architecture optimization in nanotwinned ceramics.

Structural ceramics are commonly used in extreme environments, such as aerospace thermal barriers, turbine engines, biomedical implants, and cutting tools. Such service environments require stricter combinations of strength, thermal stability, and damage tolerance[1–3]. However, rigid covalent/ionic bonding and limited capability for dislocation nucleation and multiplication usually result in their inherent brittleness at room temperature. Consequently, these constraints often lead to catastrophic failure under an unbearable load. Overcoming this brittleness while preserving or enhancing the strength of ceramics represents a grand challenge in materials science. Recent approaches, such as introducing pre-existing dislocations[4,5] or softer phases[6,7], have made some progress but typically compromise yield strength. Recently, an intrinsic strategy using point-defect superstructuring has been shown to reduce dislocation nucleation barriers, achieving metallic-like ductility without sacrificing hardness in refractory nitrides. Thus, developing intrinsic mechanisms that simultaneously enhance strength and ductility holds great potential for next-generation ceramics.

In alloys, TWIP and TRIP effects enabled breakthroughs in automotive safety and aerospace components[8–10] by synergistically

[1]Erich Schmid Institute of Materials Science, Austrian Academy of Sciences, Jahnstraße 12, Leoben A-8700, Austria. [2]Institute of Materials Science and Technology, TU Wien, Vienna A-1060, Austria. [3]Christian Doppler Laboratory for Surface Engineering of high-performance Components, TU Wien, Vienna A-1060, Austria. [4]Department of Materials Science, Montanuniversität Leoben, Franz-Josef-Straße 18, Leoben A-8700, Austria.
e-mail: zaoli.zhang@oeaw.ac.at

enhancing ductility, work hardening, and fracture resistance. Can we extend paradigms like TWIP and TRIP from metals to ceramics? In ceramics, extensive investigations into the strain-induced tetragonal→monoclinic transformation in ZrO_2-based ceramics have succeeded in enhancing toughness and plasticity over the past few decades[11–13]. Furthermore, the α → β transformation and subsequent bonding switch in Si_3N_4 also achieve 20% room-temperature plasticity in covalently bonded ceramics[14]. Recently, advanced machine-learning interatomic potentials robustly predict stress-induced phase transformations in refractory ceramics[15,16]. These simulations reveal that tailored shear or uniaxial strains can activate nanoscale transformations, thereby reducing yield stresses and dissipating energy[16]. However, translating these predictions into realized material properties faces critical experimental gaps. Synthesizing phase-pure metastable polymorphs, controlling stoichiometry and defects, and performing in situ micromechanical tests coupled with high-resolution structural characterization under complex loading all present significant challenges. In contrast, the TWIP effect in ceramics has rarely been reported due to the inherently high stacking fault energy of most ceramics. A recent study on an ultrahard single-crystal cubic BN[17] revealed significant deformability enabled by deformation twinning and proved the great potential of TWIP in improving the ductility of ceramics. However, achieving synergy between TWIP and TRIP in ceramics remains underexplored, despite its potential importance.

Here, we demonstrate the synergistic activation of the TWIP and TRIP mechanisms in monolithic δ-TaN, a representative transition-metal nitride (TMN) ceramic. First-principles calculations indicate that at 0 K, perfect stoichiometric δ-TaN resides at a local energy minimum, thereby possessing mechanical stability against rigid lattice sliding along the primary {111}<112> slip systems. Within this 0 K energy landscape, the lattice exhibits an intrinsically negative stacking fault energy, indicating a profound theoretical driving force for planar faulting[18,19]. Although the phase still exhibits imaginary phonon frequencies, rendering it dynamically unstable with respect to lattice vibrations at absolute zero, strong anharmonic lattice vibrations dynamically stabilize the cubic phase at elevated temperatures[20]. The dynamically stabilized phase effectively preserves its inherent propensity for faulting, favoring the profuse activation of stacking faults and deformation twinning, as observed in experiments[21,22]. Consequently, δ-TaN presents an ideal model system for investigating TWIP and TRIP effects in ceramics. Through an integrated approach combining micro- and nano-mechanical testing, extended atomic-level quantitative characterization by transmission electron microscopy (TEM), and ab initio molecular dynamics (AIMD) simulations, we resolved prior synthesis and characterization challenges and revealed that TWIP and TRIP operate successively under stress in the TaN thin film. This dual-mechanism activation achieves remarkable plasticity and strength enhancement in the polycrystalline ceramic, effectively helping an ultrahard ceramic acquire metal-like damage tolerance. These findings offer a perspective on overcoming the strength–ductility trade-off in monolithic ceramics.

Results

Synthesis and microstructure

We employ direct current reactive magnetron sputter deposition (Fig. 1a) and exploit the optimized parameters to kinetically trap the high-temperature face-centered cubic (FCC) polymorph. In the Ta–N system, hexagonal ε-TaN (NiAs-type) is the thermodynamically stable phase at room temperature and ambient pressure, while hexagonal θ-TaN (WC-type) is typically synthesized under high-pressure conditions[23,24]. The cubic δ-TaN (NaCl-type, B1) is a high-temperature phase. Under the highly non-equilibrium conditions of reactive magnetron sputter deposition, however, phase formation is governed not solely by equilibrium thermodynamics but by a competition between thermodynamic driving forces and kinetic factors. Systematic investigations by Shin have established a phase map for reactively sputtered TaN_x layers, showing that metastable B1 δ-TaN_x is the dominant phase over a wide temperature range. Building on these insights and our prior work, we selected a deposition temperature of 700 °C with a proper N_2 partial pressure and total working pressure to favor the nucleation and growth of δ-TaN. The metastable δ-TaN is successfully deposited under these deposition conditions, as confirmed by X-ray diffraction (XRD) showing exclusive (111) and (002) FCC reflections (Fig. 1b). Compared with our previous study[22], we found that the crystallographic texture and twin morphology of TaN films on Al_2O_3(0001) substrates exhibit profound dependence on deposition energetics. Under floating substrate conditions[22], low-energy ion bombardment maintains (111)-oriented epitaxy, promoting abundant Σ3 coherent twin boundaries (CTBs) parallel to the growth interface (the Σ3 notation refers to a coherent {111} twin interface with the two grains related by a 60° rotation about the ⟨111⟩ axis normal to the interface). In this study, we adopted fixed-bias deposition at −50 V and triggered a thickness-dependent texture transition: the film below 100 nm retains a (111) orientation, whereas beyond this critical thickness, the accumulated strain energy drives reorientation to a (001) fiber texture (Fig. S1a). This transition was verified by cross-sectional selected area electron diffraction (SAED) measurements, in which the diffraction spots from the original epitaxial (111)-oriented growth and twinning are gradually replaced by intense 002 reflections (Fig. S1b, c). Besides, cross-sectional grain size analysis reveals a structural gradient along the growth direction (Fig. S1d), where (001) grains gradually acquired growth advantages through orientation-specified coalescence (Fig. S1e). More details about the microstructure can be found in the supplementary text and Figs. S2–S6. Besides, TEM-EDS measurements on the as-deposited film yield a composition of approximately 58 at% Ta and 42 at% N, confirming a nitrogen deficiency relative to the 1:1 stoichiometry. We should note that EDS quantification of light elements such as nitrogen is inherently uncertain. This off-stoichiometry is consistent with the defect-stabilization mechanism identified by Koutná et al.[25] and Klimashin et al.[26], wherein nitrogen and/or metal vacancies lower the formation energy of the cubic phase.

We further investigated the defect structure of the as-deposited film with scanning transmission electron microscopy (STEM) and high-resolution TEM (HRTEM). Within the dominant (001)-oriented grains (the SAED pattern in Fig. 1c), a complex nanotwin architecture emerges through the synergistic accumulation and interaction of twin boundaries (TBs) and stacking faults (SFs) on inclined {111} planes. Aberration-corrected HRTEM images (Fig. 1d, e) reveal the development of primary Σ3 twin boundaries (TB_{I}) that host finer secondary nanotwins (TB_{II}). The fast Fourier transform (FFT) in Fig. 1d (inset) confirms the crystallographic relationships of this hierarchical architecture, while the annotations in Fig. 1e directly identify the primary and secondary twins within the structure. As schematically summarized in Fig. 1f, unlike conventional nanotwinned structures, in which TBs are predominantly parallel and unidirectional, the hierarchical nanotwinned architecture creates a three-dimensional interlocking network of twin boundaries oriented on multiple {111} planes. These hierarchical nanotwin networks induce profound grain refinement and reorientation by subdividing grains into parallelogram domains. We designate this microstructure as hierarchical nanotwinned TaN (abbreviated as 'hnt-TaN'), characterized by its multi-scale twin networks. This terminology distinguishes it from our previously reported nt-TaN/TiN superlattice[22], which was fabricated at 700 °C without an applied bias.

Mechanical properties

To assess how different nanotwin architectures influence the mechanical properties, we performed room-temperature uniaxial micro-pillar compression tests on both nt-TaN/TiN and hnt-TaN

https://doi.org/10.1038/s41467-026-79377-w

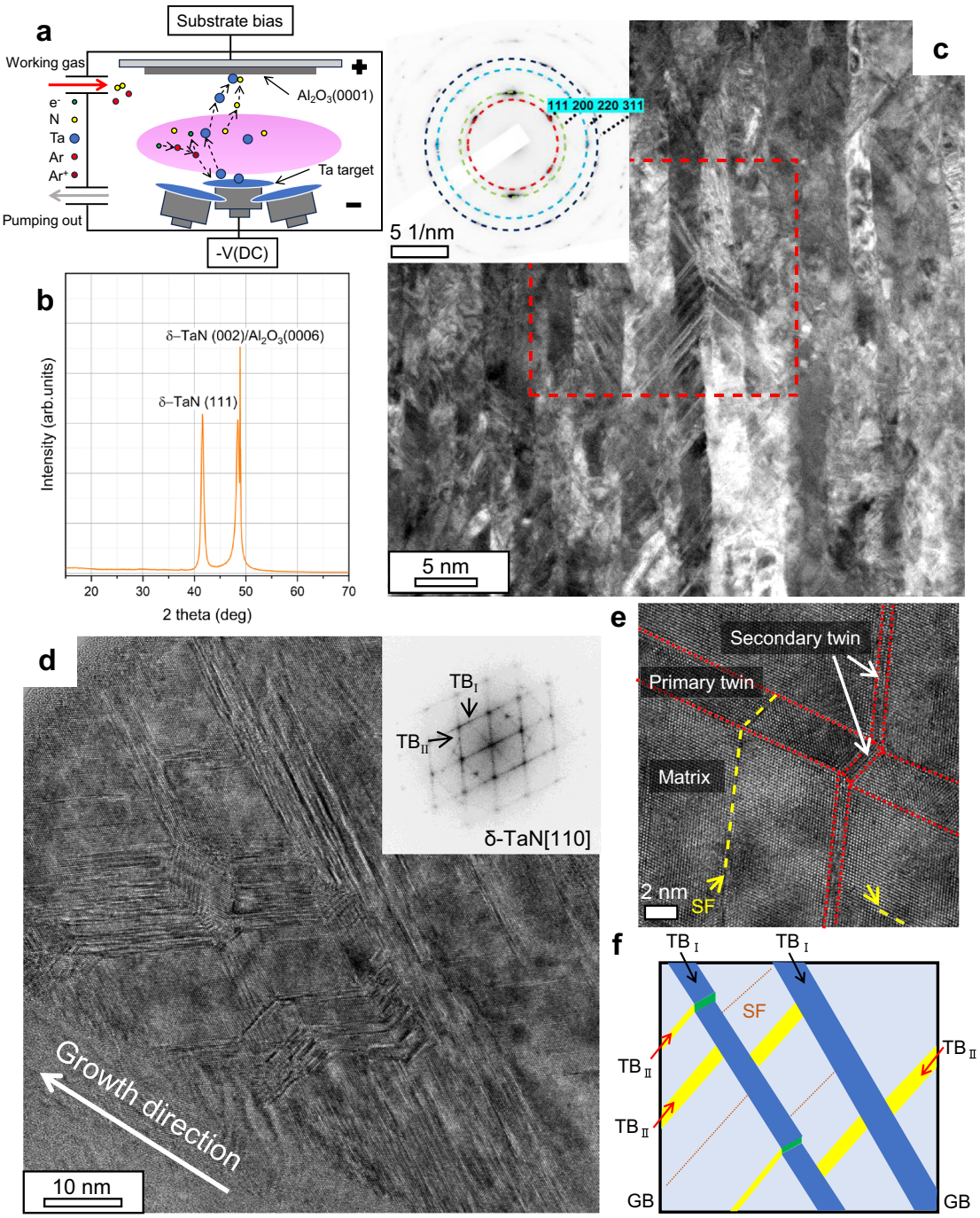

Fig. 1 | Synthesis and hierarchical nanotwin structure of δ-TaN. a Schematic of direct-current (DC) reactive physical vapor deposition setup. **b** XRD pattern acquired using Co Kα radiation (λ = 1.790 Å), confirming exclusive FCC δ-TaN phase with (111) and (002) reflections. **c** Cross-sectional STEM image showing hierarchical nanotwin networks in (001)-oriented grains. Inset: Corresponding SAED pattern from the marked region, revealing the out-of-plane [001] texture. **d** Aberration-corrected HRTEM image of the hierarchical nanotwin structure. Inset: FFT from the hierarchical nanotwin region, identifying primary twin boundary (TB_I) and secondary twin boundary (TB_{II}) reflections. **e** HRTEM image with annotations delineating the primary and secondary nanotwins within the hierarchical architecture. **f** Schematic model of the multi-scale twin architecture (Σ3 boundaries), illustrating the structure of TB_I (marked by black arrows and represented by blue color), TB_{II} (marked by red arrows and represented by yellow color), grain boundary (GB, black color), and stacking faults (SF, brown dotted line). The observations in (**c**–**e**) were reproduced in three separately prepared TEM lamellae from the same film, all showing similar features.

(Fig. 2a, b). The nearly identical dimensions and columnar grain morphology in both films help us rule out enhanced deformability brought by size and single-crystal effects. While both exhibit similar yield strengths (11 ~ 12 GPa) and yield strains (6.1–6.8%), their post-yield responses diverge dramatically. The nt-TaN/TiN pillars undergo typical brittle fracture soon after yielding (0.2% strain) and lose load-bearing capacity immediately upon fracture (inset in Fig. 2a). In stark contrast, the hnt-TaN pillars sustain a large plastic deformation, maintaining structural integrity to over 60% engineering strain (Fig. 2b). Crucially, from yield to an engineering compressive strain of 62%, the calculated true stress increases from approximately 11.3 to 13.5 GPa, corresponding to a true strain hardening of ~2.4 GPa. This

https://doi.org/10.1038/s41467-026-79377-w

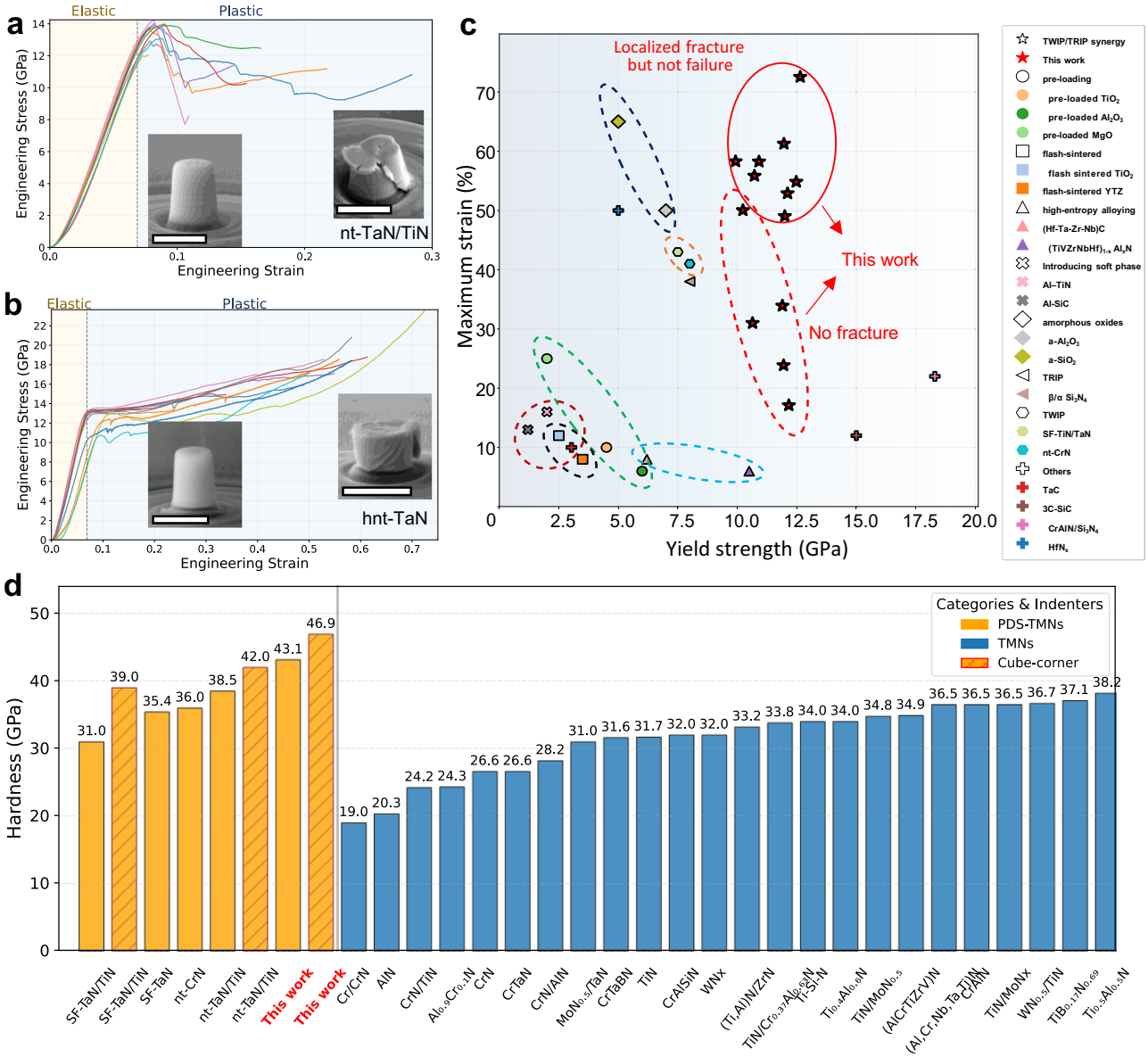

Fig. 2 | Superior room-temperature plasticity of ultrahard hnt-TaN. **a** Engineering stress-strain curve of nt-TaN/TiN pillars, exhibiting typical brittle fracture soon after yielding ($\sigma_y \approx 12$ GPa, $\varepsilon_y \approx 6.1\%$). *Inset:* Post-compression SEM image showing catastrophic failure. **b** Engineering stress-strain curve of hnt-TaN pillars, demonstrating exceptional plastic deformation tolerance with sustained load-bearing capacity up to 60% engineering strain and prominent work hardening (flow stress increases by ~6 GPa, 50% above yield). *Inset:* SEM image of the heavily deformed pillar without macroscopic fracture. (scale bar: 1 μm). Each colored trace in (**a**). **b** corresponds to an independent micropillar compression test ($n = 7$ for nt-TaN/TiN and $n = 12$ for hnt-TaN). Source data are provided as a Source Data file. **c** A comparison of the mechanical performance of hnt-TaN with other state-of-the-art strategies for enhancing the room-temperature plasticity of ceramics[4,5,14,21,27–37]. Our hnt-TaN, which leverages the synergy of TWIP and TRIP effects, occupies a unique region of high strength and large compressive strain. **d** Hardness comparison of hnt-TaN with other transition metal nitrides (TMNs)[36,55–74]. The monolithic hnt-TaN film achieves a peak hardness of 43.1 GPa, which not only leads the category of planar-defect-strengthened (PDS) nitrides but also surpasses TMNs strengthened by complex strategies such as nanolaminates and multi-component alloying. Detailed values and full references for all comparative data points are compiled in Supplementary Tables S1 and S2.

performance is highlighted in the context of recent advances in ductile ceramics (Fig. 2c, details in Table S1)[4,5,14,21,27–37]. Our hnt-TaN exhibits an exceptional combination of high compressive strain capacity and yield strength, surpassing the conventional trade-off boundaries. Notably, one hnt-TaN micropillar with a yield strength of ~10 GPa reached 52% strain without crack formation (inset of Fig. 2b and Movie S1). Similarly, the deformed pillars consistently exhibit the formation of multiple, distributed shear bands with higher strains rather than localizing to a single catastrophic fracture plane (Fig. S7). Moreover, even in pillars where micro-cracks did initiate, the cracks did not propagate catastrophically. Instead, as captured in situ Movie S2, crack bridging occurred following micro-crack propagation, and the pillars retained complete load-bearing and working hardening capacity after cracking. This remarkable damage tolerance stands in sharp contrast to the immediate failure of nt-TaN/TiN.

We further conducted nanoindentation tests to evaluate the hardening efficacy of hierarchical nanotwinning. Under identical conditions, monolithic hnt-TaN exhibits a peak hardness of 43.1 GPa and a concurrently elevated elastic modulus (Fig. S8). Representing a 12% to 40% enhancement over other planar-defect configurations like nanotwinned superlattices (nt-TaN/TiN: 38.5 GPa) and stacking-fault-strengthened films (SF-TaN: 35.4 GPa; SF-TaN/TiN: 30.7 GPa), this

performance also extends well beyond the typical range reported for TMNs (19–38 GPa) (Fig. 2d). For broader contextualization, hnt-TaN is competitively positioned against other leading protective coating materials (Fig. S9, details in Table S2). Together, these results demonstrate that unlocking TWIP/TRIP synergy via hierarchical nanotwinning offers a potent strengthening pathway in compositionally simple binary systems, rivaling both complex multicomponent ceramics and multilayer designs.

The residual impressions (Fig. S10) after indentation show pronounced material pile-up in hnt-TaN, indicating substantial shear-driven plasticity during deformation. This ductile character is coupled with improved crack resistance: radial cracks in hnt-TaN are ~18.2% shorter, indicating a higher apparent fracture resistance than that of nt-TaN/TiN. It should be noted that the different bias voltages may introduce residual stresses that partly contribute to the higher apparent fracture resistance[38]. Together, these results indicate that hnt-TaN achieves a balance of ultrahigh hardness and damage tolerance.

Strain-dependent deformation mechanism

To uncover the mechanism of the enhanced plasticity and strengthening, we investigated the deformed pillars (Fig. S7a, b) and found that the deformation of hnt-TaN follows strain-dependent pathways, transitioning from twin- and dislocation-mediated plasticity at low-to-moderate strains to mechanisms involving phase transformation at higher strains.

To capture the microstructural evolution at the onset of plastic flow, we unloaded and examined a micropillar compressed to a strain of ~18.2%, corresponding to the early stage of the post-yield stress plateau (Fig. 3a, Fig. S7a). At this low strain, we revealed that the microstructural evolution of hnt-TaN is driven by twin refinement and dislocation accumulation. The deformed pillar maintains an FCC structure while achieving gradual columnar grain bending, evidenced by broader 001 diffraction arcs ($\Delta\alpha = 25°$ versus 17.5° in the as-deposited film) (Fig.3b) and a DF STEM image (Fig.3c). Dark-field TEM analysis (Fig. S11), which contrasts the microstructure before and after deformation, reveals a substantial increase in dislocation density and the development of a terraced morphology near columnar grain boundaries post-deformation. Bright-field (BF) TEM imaging (Fig. 3d) shows the defect structure of a bent grain. Atomic-resolution analysis of the region (Fig. 3e, Fig. S12a–d) captures active twin subdivision, where Shockley partial dislocations ($1/6 < 112 > \{111\}$) gliding on intersecting {111} planes generate a higher density of TB_{II} within primary twin domains (indicated by white arrows in Fig. 3e). Quantitative post-deformation HRTEM analysis (Fig. S12e) shows that the mean twin thickness decreases by ≈36% compared to the as-deposited state (from 5.29 nm to 3.40 nm). Many of these TB_{II} are incompletely developed, terminating within the matrix and creating terraces along primary boundaries. Geometric phase analysis (GPA) confirms that the terminating TB_{II} structures introduce pronounced local strain field variations (Fig. 3f, ε_{xx} map). Concurrently, the formation of multi-fold twinning structures, including Σ3 and Σ27 boundaries, further accommodates the large strain (Fig. S12f). Consequently, mechanical twinning accommodates early-stage strain while dynamically refining the microstructure via twin subdivision (Fig. 3h).

At extreme engineering strains (≈60%), hnt-TaN maintains a remarkable load-bearing capacity despite localized cracking (Fig. 2b and Fig. S7b). Beyond the further densified twin/stacking fault network (Fig. S13), comprehensive diffraction analysis reveals a phase transformation through anomalous reflections between 200 and 220 diffraction rings of δ-TaN (Fig.4b). Dark-field imaging (Fig.4c) obtained by selecting the new diffraction (as marked) showed that these transformation products distribute diffusely throughout the micropillar while showing preferential concentration in high-strain regions (near the top and fracture). HRTEM imaging (Fig. 4d) further reveals the atomic-scale lattice structure of the transformed zones, while GPA of the shear strain (ε_{xy}) shows pronounced distortion along inclined {111} planes (Fig. 4e). Convergent-beam electron diffraction demonstrates streaked superlattice spots along <111> directions (Fig. 4f), collectively indicating a continuous shear-mediated transformation pathway. A detailed atomic-resolution investigation (Fig. 4g) further uncovers the transformation mechanism. By coordinated atomic displacements along $<112> \{111\}$ directions with variable Burgers vectors, FCC δ-TaN progressively transforms into hexagonal θ-TaN. Meanwhile, some metal-terminated twin boundaries (CTB_m) evolved into nitrogen-terminated twin boundaries (CTB_{nm}, the subscript 'nm' stands for non-metal) (see Fig. S14h, i). The phase transformation is mediated by a continuum of transitional crystal structures that bridge the parent δ-TaN and the product θ-TaN. These states accommodate deformation through progressive lattice distortion, thereby enabling a shear-mediated transformation without abrupt phase boundaries. A statistical analysis (Fig. S15) of atomic-resolution images reveals that the transformation proceeds through anisotropic yet coordinated lattice distortions, rather than a direct jump between well-defined phases. This collective atomic shuffling, also quantified by bond-angle rotation (Fig.4h), constitutes the TRIP effect in the ceramic system. Similar to its role in metallic alloys[8], this displacive transformation effectively accommodates shear strain and enhances ductility.

Notably, this phase transformation is not exclusively stress-driven; localized electron-beam excitation triggers identical structural evolution (Fig. S16), confirming that the activation barrier is accessible via external energy input independent of mechanical loading.

Ab initio molecular dynamics simulation

Next, we track the origin of hnt-TaN that exhibits the enhanced plasticity by means of AIMD simulations, to tackle two critical questions: What enables the remarkable plasticity in [001]-textured hnt-TaN, and why does [111]-textured nt-TaN/TiN remain brittle? To this end, we simulated shear along $\{111\}\langle 112\rangle$in defect-free and nanotwinned TaN (with CTB_m and CTB_{nm}) to elucidate the role of TBs in TWIP and TRIP. Besides, given that fracture is often initiated by tensile-stress accumulation[39], we also conduct AIMD uniaxial elongation simulations perpendicular to the TBs. These simulations are explicitly designed to probe the severe mechanical anisotropy of the twinned architecture and to unveil the intrinsic fracture response when shear-mediated pathways are geometrically suppressed. To capture such brittle cleavage at the atomic scale, which cannot be faithfully reproduced by compression due to periodic boundary constraints, AIMD tensile loading serves as a standard probe for correlating theoretical toughness with fracture-resistance statistics collected by experimental testing[40].

The simulations revealed dramatically different mechanical responses under shear versus tensile loading. Under shear loading, the nanotwinned structure demonstrated nearly half the yielding strength (~18.7 GPa for CTB_m and ~14 GPa for CTB_{nm}) alongside enhanced plasticity compared to defect-free TaN (≈32 GPa) (Fig. 5a). Conversely, tensile loading perpendicular to TBs showed high and similar yield stress (29–33 GPa) (Fig. 5b) across all configurations. This pronounced contrast confirms that nanotwins selectively enhance plasticity when shear activates $\{111\}\langle 112\rangle$slip, consistent with experimental observations (Figs. 3e, 4d). To uncover the mechanisms behind this divergent behavior, we deciphered the atomic-level deformation pathways.

(1) In defect-free TaN, shear loading induced a homogeneous lattice transformation through coordinated atomic shuffling (Fig. 5c, Movie S3). Quantitative analysis of the atomic trajectories, including radial distribution functions and bond angle distributions, confirms a continuous transformation from an FCC to a hexagonal stacking sequence (see Fig. S17a, b, and their notes for more details). Collectively, these signatures confirm a gradual transformation of the FCC

https://doi.org/10.1038/s41467-026-79377-w

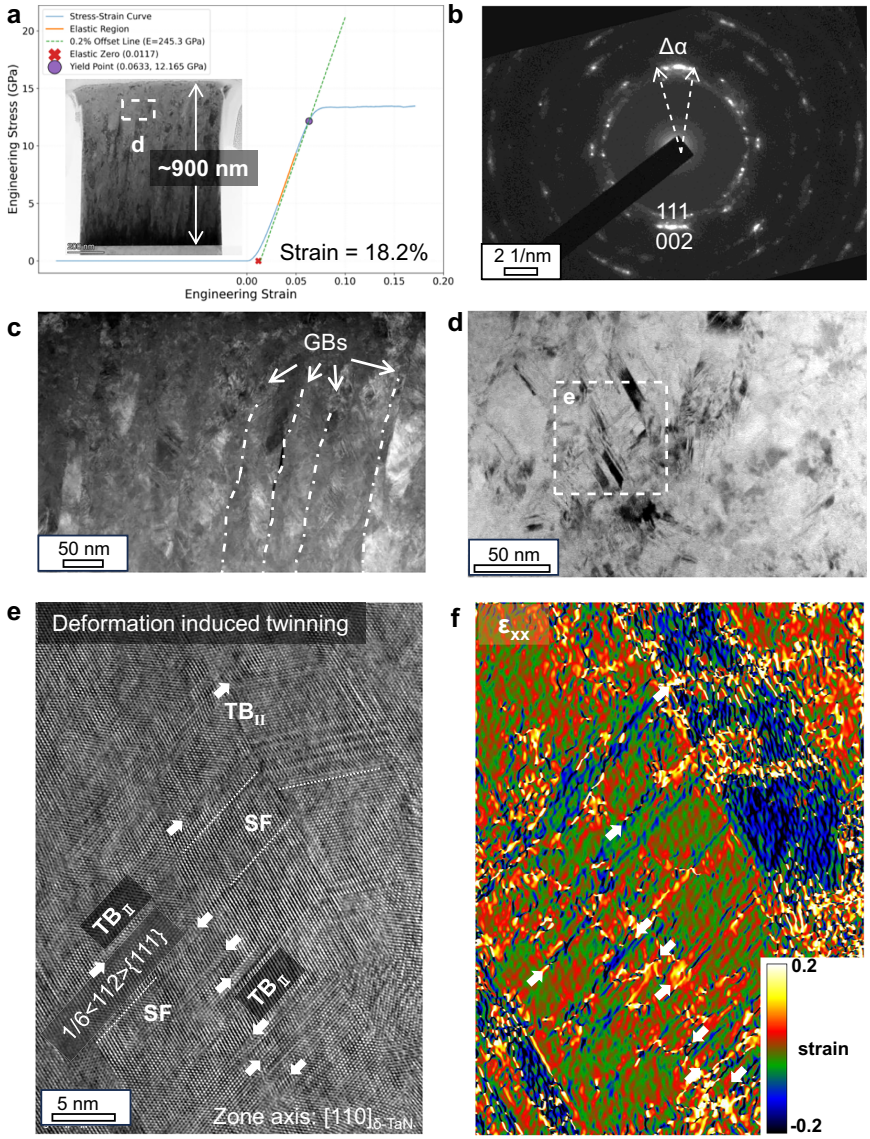

Fig. 3 | Deformation mechanisms of hnt-TaN at low strain (ε = 18.2%). a BF STEM image of the deformed micropillar with the corresponding engineering stress-strain curve. The dashed box indicates the specific region shown in (**d**). **b** XRD pattern from the deformed pillar, showing broadened 001 diffraction arcs (Δα = 25°) compared to the as-deposited state (Δα = 17.5°) and lattice rotation. **c** DF STEM image revealing bent columnar grains, with selected grain boundaries (GBs) annotated to highlight their curvature. **d** BF TEM image acquired under near two-beam condition with **g** = 111. **e** HRTEM image of the region marked in (**d**), showing an increased density of secondary nanotwins (TB_{II}) connected to a primary twin boundary (TB_{I}) on one side only. **f** GPA map of in-plane strain (ε_{xx}) reveals strong strain field variations localized at these terminating TB_{II}. The low-strain deformation was repeated on $n = 3$ independent micropillars, and TEM lamellae from these specimens showed similar deformation features. **a**, **c**, **d**, **e** are representative examples.

lattice into a rectangular configuration along the [110] projection, consistent with experimental HRTEM measurements (Fig. 4g, h). However, this transformation is unsustainable under large strains; once the shear strain reaches 28%, the defect-free lattice reaches its theoretical shear strength and undergoes catastrophic lattice slip (see Movie S3). Rather than physical cleavage, the system accommodates further deformation through intense strain localization. The massive shear displacement becomes highly concentrated along specific (111) planes, leading to localized structural destabilization, while the surrounding crystalline regions undergo elastic unloading. This atomistic strain localization directly accounts for the precipitous stress drop observed in the simulated stress-strain curve.

(2) In stark contrast, deformation in CTB_m structures proceeded through a sustainable cascade of boundary-mediated events that postponed the phase transformation and the catastrophic failure (Fig. 5d, Movie S4). This process is initiated when shear-induced distortions become localized asymmetrically near the twin boundary up to a strain of 12%. Then, at a 14% strain, the CTB_m configuration transformed into CTB_{nm}, accompanied by interfacial relaxation that absorbed nearby accumulated strain energy, causing the adjacent partially transformed region to revert to the FCC structure. Subsequently, at a 16% strain, the boundary reverted to the CTB_m configuration while migrating upward by one atomic layer. The TB migration further relieved local stresses and was corroborated by fluctuations in the (111) interplanar spacing (Fig. S18). Next, at a 22% strain, additional TB migration propagated downward from the upper model surface. This cyclic sequence of distortion-mediated reversible transformation, TB transformation, and migration enabled continuous deformation without fracture. Moreover, the TB migration concurrently reduces twin spacing, thereby freeing up volume for additional TB

https://doi.org/10.1038/s41467-026-79377-w

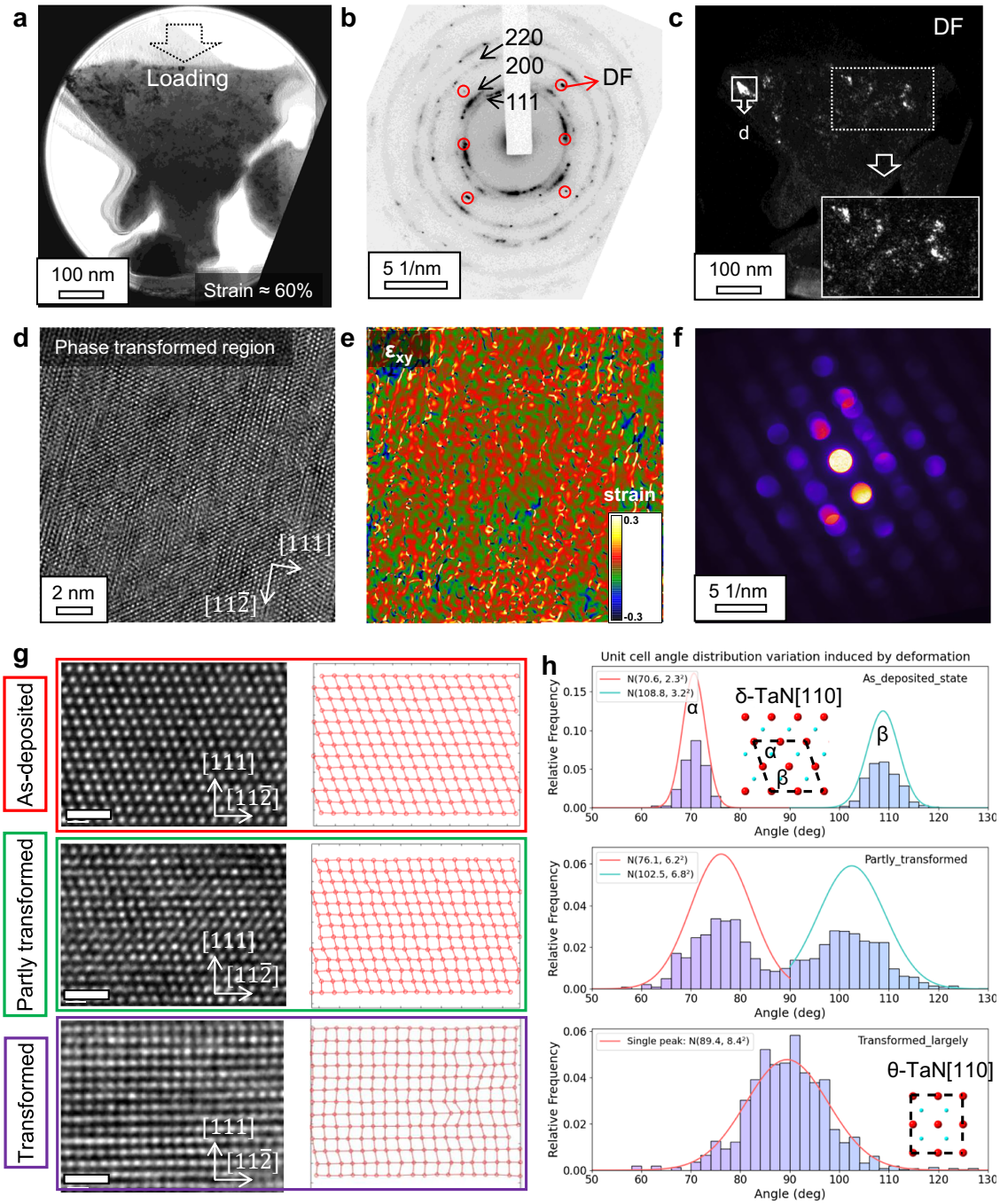

Fig. 4 | Strain-induced phase transformation of hnt-TaN at high strain (ε ≈ 60%). a BF TEM image of the heavily deformed pillar (cut from the region indicated in the right inset of Fig. S10b). The arrow indicates the loading direction. **b** SAED pattern, revealing anomalous reflections (red circles) between the primary 200 and 220 rings of the FCC δ-TaN phase, indicating a stress-induced transformation. **c** DF TEM image formed from the new reflections, showing the transformation products distributed throughout the pillar with preferential concentration in high-strain regions. The inset magnifies the dashed area. **d** Atomic-resolution HRTEM image from a transformed region in (**c**). **e** GPA map of shear strain (ε_{xy}) derived from (**d**), showing pronounced distortion along the inclined {111} planes. **f** Convergent-beam electron diffraction pattern with streaked superlattice spots along the <111>*, indicating a continuous shear-mediated transformation. **g** Atomic-scale progression from as-deposited δ-TaN (top) to a partially transformed intermediate state (middle) and almost fully transformed region (bottom). The red overlays on the right show fitted Ta atomic positions from the corresponding HRTEM images; only Ta columns are resolved, and all images were acquired along the [110] zone axis of the parent phase. **h** Bond-angle distribution showing the transition from a bimodal distribution (peaks at ~70.5° and ~109.5°, characteristic of FCC symmetry) in the as-deposited state to a unimodal distribution centered at 90° (hexagonal WC-type structure) in the fully transformed state. Source data are provided as a Source Data file. The large-strain deformation was repeated on $n = 9$ independent specimens, and TEM analyses of these specimens showed similar features; (**a**), (**c**) and (**d**) are representative examples.

https://doi.org/10.1038/s41467-026-79377-w

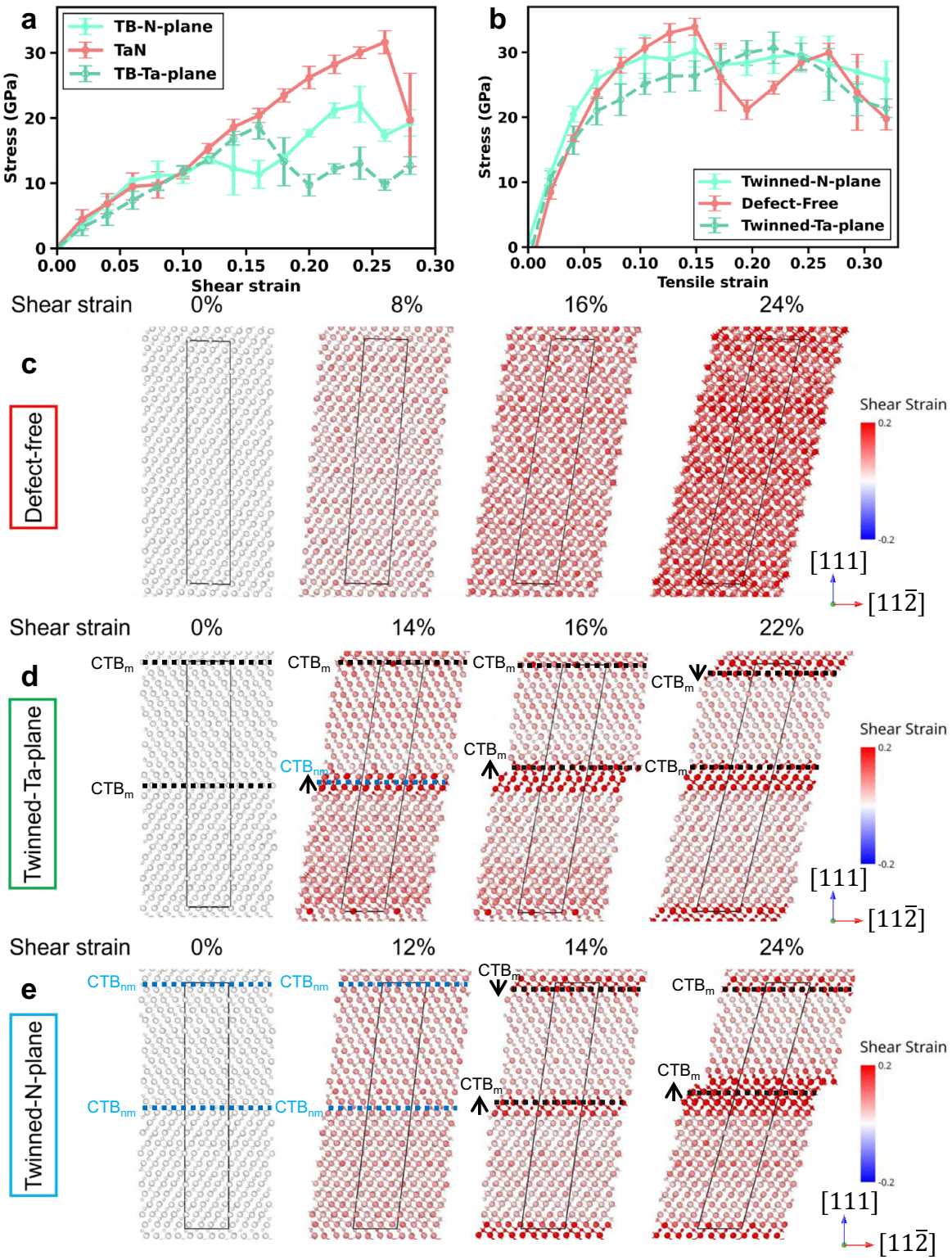

formation. By continuously iterating this cycle, alternating between a storage stage (matrix distortion) and a release stage (TB migration), the twinned architecture establishes a remarkably steady-state plastic flow during subsequent deformation. A comprehensive analysis of this structural transformation behavior and the associated stress evolution at extended shear strains (exceeding 30%) is detailed in the Supplementary Text and Fig. S19.

(3) Parallel simulations of CTB_{nm} structures revealed analogous mechanisms but with accelerated transformation kinetics (Fig. 5e, Movie S5), where CTB_{nm} reverted to CTB_m at 12% strain. Thus, our simulations reveal a self-regulated deformation sequence at the

Fig. 5 | Atomistic mechanisms of synergistic TRIP/TWIP activation in nanotwinned TaN. a Shear stress-strain responses for defect-free and twinned TaN. **b** Tensile stress-strain curves perpendicular to TBs. The plotted stress values in (**a**). **b** are the mean values calculated over the final 500 steps of each 2 ps NVT simulation at 300 K. Error bars represent the standard deviations of the instantaneous stress values over these 500 steps. Each deformation condition was simulated using a single AIMD trajectory without repetitions. **c** Uniform lattice distortion and progressive FCC→hexagonal transformation in defect-free TaN under shear, visualized through shear strain distribution (see Movie S3). **d** Deformation process in CTB_m under shear. Before 14% strain, shear strain accumulates. At 14% strain, CTB_m transforms to CTB_{nm}, forming a localized transformed layer. At a 16% strain, an inverse transformation (CTB_{nm}→CTB_m) occurs, accompanied by upward TB migration, reverting the distorted lattice back to FCC and releasing local strain. At 22% strain, further stress relief is achieved via downward TB migration (see Movie S4). **e** Accelerated transformation in CTB_{nm}, where spontaneous reversion to CTB_m occurs at 12–14% strain, corresponding to the early stress drop in **a**), followed by boundary migration (see Movie S5) to a fully transformed state. (Note: Strain values on the plotted axes in **a**, **b** and the local shear strain color scale in c-e are expressed as fractional strains, where a value of 0.1 corresponds to 10% strain).

atomic scale: strain-induced phase transformation at TBs is punctuated by TB migration events that release local stress concentrations. This cyclic process is fundamental to the sustained plasticity observed in twinned ceramics.

Having established the atomic-scale origins of shear-mediated plasticity, we now turn to the contrasting case of tensile deformation. This is also essential to understand the brittle response of nt-TaN/TiN. Under uniaxial tensile loading perpendicular to TBs, both twinned and defect-free structures exhibited fundamentally distinct deformation pathways compared to shear conditions. Notably, we observed no phase transformation or twin boundary migration analogous to the shear-mediated processes (Fig. S20). Instead, accumulated lattice distortions led to localized fracture in all configurations once critical strain thresholds were reached. Crucially, defect-free TaN initiated fracture at approximately 15% strain, with crack propagation causing progressive structural destabilization. By contrast, twinned structures demonstrated enhanced structural integrity, delaying the onset of fracture to higher strains (18-20%) and maintaining load-bearing capacity throughout deformation. This preservation of coherence stems from twin boundaries acting as barriers to crack propagation, effectively redistributing local stresses—a phenomenon that is particularly pronounced in CTB configurations where fracture surfaces preferentially follow zigzag paths along interfaces. This simulation evidence of interface-induced crack tortuosity directly substantiates the intrinsic capacity of nanotwinned architectures to mitigate catastrophic crack propagation, thereby indirectly validating their positive contribution to the fracture toughness of the nanotwinned ceramic system.

Collectively, our AIMD simulations provide a unified atomistic rationale for the divergent macroscopic behaviors. The remarkable plasticity of hnt-TaN originates from shear-mediated TB migration and phase transformation. In contrast, the brittleness of nt-TaN/TiN is governed by a stress state predominantly perpendicular to the TBs, which suppresses shear-mediated mechanisms and leads to brittle failure.

Multiscale synergistic strengthening and plasticity mechanisms

Finally, we elucidate the underlying mechanisms that govern the excellent mechanical properties of hnt-TaN ceramics. The remarkable ductility and hardness enhancements of hnt-TaN at room temperature arise from a multiscale coupling between its hierarchical nanotwin architecture and the TWIP and TRIP mechanisms. Unlike conventional approaches, which often compromise strengthening or plasticity, these mechanisms are integrated and cooperative across multiple scales.

At the atomic scale, AIMD simulations reveal a dynamic interplay between deformation twinning and phase transformation that is coupled through a self-regulating cycle. Under shear loading along {111} planes, reversible switching between CTB_m and CTB_{nm} configurations substantially lowers the threshold for plastic deformation. Subsequent TB migration not only releases stored energy and postpones phase transformation, but also refines the twin spacing, consistent with (HR)TEM observations of terracing (Fig. 3e) and (111) lattice-spacing fluctuations (Fig. S13). As strain escalates beyond a critical threshold, this mechanism is progressively supplemented and then succeeded by the TRIP effect. Stress concentrations activate the FCC→hexagonal phase transformation. This transformation accommodates massive strain through a continuum of distortion, coordinated atomic shuffling, and bond-angle rotation, which is also essential for enhancing plasticity.

At the microscale, the mechanical response is governed by a multi-stage structural evolution. Initially, prior to macroscopic yielding, the nanoscale columnar grain boundaries impart a profound static Hall-Petch strengthening. This static size effect is the primary contributor to the ultrahigh yield strength of the polycrystalline hnt-TaN (~12 GPa), which is significantly higher than that of reference systems such as TaN/TiN superlattice (~7.5 GPa)[21] or HfN_x (~5 GPa)[41]. Subsequently, the significant strengthening of hnt-TaN is attributed to the multi-scale obstruction of dislocation motion by its hierarchical nanotwin architecture, further augmented by both TWIP and TRIP effects. While conventional nanotwin structures are well-established in effectively impeding the glide of both partial and full dislocations[22], the hierarchical network provides superior confinement by subdividing the columnar grains into finer, parallelogram-shaped blocks. Critically, this three-dimensional twin network offers potent barriers to dislocation glide on multiple intersecting {111} slip planes, unlike single-orientation nanotwins. Furthermore, the deformation process itself introduces dynamic strengthening from two synergistic sources: First, the strain-induced continuous refinement of the microstructure through the activation of secondary twinning (see Fig. 3e and Fig. S11c), dynamically reduces the mean free path for dislocations. Second, and crucially, the activation of the TRIP effect introduces a dual strengthening contribution. The transformation product, hexagonal θ-TaN, possesses a substantially higher shear modulus (~233 GPa) than the parent FCC δ-TaN (~105 GPa)[42], offering greater intrinsic resistance to dislocation glide. Concurrently, the coherent phase boundaries generated between the δ and θ phases create additional potent barriers that impede dislocation motion. This dynamic refinement and transformation-hardening effects collectively achieved the work hardening during compression.

From the atomic to the microscale, this bridge is achieved through the synergistic design of a hierarchical nanotwin architecture with a strong [001] fiber texture. The [001] texture maximizes the resolved shear stress on the inclined {111} planes, efficiently activating the shear-mediated TWIP and TRIP mechanisms that are essential for plasticity. Simultaneously, the three-dimensional hierarchical nanotwin network within the deposited film enables the effective synergy of these mechanisms. Consequently, during pillar compression, the initial strain plateau ($\varepsilon \approx 6$–15%) is governed by twin boundary migration and refinement, accommodating deformation without damage. With increasing strain, FCC→hexagonal phase transformations are activated, whose interfaces concurrently strengthen the material and accommodate further strain. At extreme strains ($\varepsilon \approx 60\%$), a coherent distortion continuum facilitates the formation of fully transformed θ-TaN, preserving structural integrity. Ultimately, this work establishes a paradigm in ceramic design, demonstrating

that the synergy of TWIP and TRIP effects within a precisely architected nanotwin framework can transcend traditional strength-ductility trade-offs, paving the way for ultrahard yet ductile ceramics. More broadly, the synergistic TWIP–TRIP mechanism demonstrated here, rooted in the hierarchical nanotwin architecture, may offer a transformative strategy for designing ceramics resilient to extreme thermomechanical demands in aerospace propulsion, advanced energy systems, and next-generation wear-resistant technologies.

Methods

Thin film synthesis

The film used in this study was prepared by direct current magnetron sputtering using a custom-made lab-scale magnetron sputter deposition system equipped with a Ta target (99.99 % purity, Ø 50.8 mm × 6 mm). The film was grown on an Al_2O_3(0001) substrate at 700 °C, and the substrate was kept at a −50V bias voltage during the deposition. Besides, the partial pressures of N_2 and Ar were maintained at 0.2 Pa and 0.6 Pa, respectively. The actual total thickness of deposited TaN was about 1.1 μm.

X-ray diffraction measurement

The overall composition and crystallographic structure of the films were characterized by X-ray diffraction (XRD) using a Bruker D2 Phaser X-ray diffractometer with Co Kα radiation with a wavelength of 1.790 Å (operated at 30 kV and 10 mA). Samples were placed on a silicon wafer to minimize the background influence. The diffraction was conducted in the range from 15° to 70° at a scanning rate of 1.625°/min.

Pole-Fig.s measurements

Laboratory X-ray diffraction (XRD) studies were performed using a Rigaku SmartLab 5-circle diffractometer, equipped with Cu Kα radiation, a parabolic multilayer mirror, a graphite monochromator, and a scintillation counter. The pole Fig. measurements were performed using Schultz reflection technique using alpha and beta steps of 1 degree.

Nanoindentation test

Indentation tests were conducted on a KLA Nanoindenter G200 equipped with diamond Berkovich and cube-corner indenter tips (Synton-MDP) to obtain hardness H and Young's Modulus E by the conventional analysis first proposed by Oliver and Pharr[43]. The tests applied the continuous stiffness measurement method with a superimposed sinusoidal signal (2 nm, 45 Hz) and a constant indentation strain rate (ε) of 0.05 s^{-1}. Six indentations were performed at each displacement (500 nm, 1000 nm) for mechanical property measurement. The hardness and elastic modulus were measured at penetration depths of 80-90 nm into the film. To qualitatively compare the fracture toughness, indentations by a cube-corner tip were performed at a maximum penetration depth of 1000 nm to generate radial cracks for crack length comparison. From each indentation, all three radial cracks were measured from the impression center to the crack tip, giving a total of 18 crack length measurements per film.

TEM sample preparation

The cross-sectional TEM lamellae of both the as-deposited film and the micro-pillars subjected to different levels of compressive strain were prepared using a focused ion beam (FIB) system (FEI Helios NanoLab 660). Micro-pillars with varying strain levels were selected to examine microstructural evolution. Prior to FIB milling, a 3-micron-thick protective carbon layer was deposited over the region of interest. The lamellae were cut along the <11-20> direction of the sapphire substrate. Trenches were cut at 9 nA, and cross sections were cleaned at 2 nA. Then, the lamella was cut and transferred to a Cu TEM grid. The lamellae were polished using accelerating voltages ranging from 30 down to 5 kV and beam currents from 2 nA down to 7 pA to minimize ion beam damage.

TEM characterization

For HRTEM characterization, JEOL 2100 F and FEI Titan Themis 60-300 cubed TEM that are both equipped with an image-side spherical aberration (Cs) corrector (CEOS GmbH) were adopted. The aberration coefficients were set to be sufficiently small before investigations. High-angle annular dark-field (HAADF) images were acquired with the camera length set as 73 mm, and the collection angle range of the ADF detector is about 79.5-200 mrad. The atomic positions in Fig.2 and Fig.4 are fitted and analyzed using Calatom (v1.2)[44] and Python scripts based on Atomap (0.4.2)[45]. Considering the importance of the effect of λ on the macroscopic performance and the distinguishing ambiguity of twins and SFs within DF images, we chose to measure the twin spacings from abundant HRTEM images.

Micromechanical tests

The pillar compression tests were performed in a Zeiss Sigma 500 VP system combined with a FemtoTools FT-NMT04 in-situ SEM nanoindenter equipped with a flat punch (5 μm diameter) diamond tip capable of applying 200 mN at a noise level of <5 μN (measured at 10 Hz). The tests were carried out at room temperature in displacement-controlled mode with a displacement rate of 5 nm/s. The recorded load-displacement curves were used to calculate the engineering stress following an approach by Wheeler and Michler[46], where the top diameter of the pillar is taken as the reference contact area. The engineering strain was obtained from the displacement data with the coating thickness used as the initial pillar height reference. Moreover, the displacement data was corrected by accounting for the base compliance following Sneddon's correction[47] given by:

$$\Delta L = \frac{1-\nu_{sub}^2}{E_{sub}} * \frac{F}{d} \tag{1}$$

where ν_{Sub} and E_{Sub} are the Poisson's ratio and Young's modulus of the substrate, respectively, $\nu_{sub} = 0.27$, $E_{sub} = 410$ GPa (mp-1143)[42]. F is the applied force, and d is the diameter of the pillars. ΔL is then the deformation of the substrate induced by the pillar and must be subtracted before the calculation of the strain.

To exclude size effects, both nt-TaN/TiN and hnt-TaN micropillars were prepared with nearly identical dimensions.

The true stress–true strain response was estimated from the measured engineering stress–strain data under uniaxial compression. The true strain was calculated according to:

$$\varepsilon_{true} = \ln\left(1+\varepsilon_{eng}\right) \tag{2}$$

where ε_{eng} is the engineering strain (negative in compression).

To estimate the true stress, the change in cross-sectional area during deformation was accounted for. Assuming homogeneous deformation, isotropic material behavior, and a constant Poisson's ratio ν, the lateral strain was approximated as:

Accordingly, the instantaneous cross-sectional area A was expressed as:

$$A = A_0(1-\nu\varepsilon_{eng})^2 \tag{3}$$

where A_0 is the initial cross-sectional area. The true stress was then obtained from:

$$\sigma_{true} = \frac{\sigma_{eng}}{(1-\nu\varepsilon_{eng})^2} \tag{4}$$

where σ_{eng} is the engineering stress. In the present analysis, a Poisson's ratio of $\nu = 0.25$ was used. It should be noted that the calculated true stress represents an approximation, as effects such as strain-dependent Poisson's ratio, friction-induced barreling, and local deformation heterogeneity were not explicitly considered.

Calculation methods

Ab initio molecular dynamics simulations were carried out using the Vienna Ab-initio Simulation Package (VASP)[48]. Electronic interactions were treated with the projector augmented wave (PAW) formalism[49] and the Perdew--Burke--Ernzerhof form of the generalized gradient (GGA-PBE)[50]. All calculations employed a plane-wave basis with Gamma-point sampling of the Brillouin zone, a plane-wave cutoff energy of 300 eV was used. The electronic structure was converged to an accuracy of 10^{-5} eV at each ionic step. A time step of 1-fs was used to integrate the equations of motion.

The supercells were constructed from the FCC TaN motif and contained 288 Ta and 288 N atoms, giving a total of 576 atoms. The simulation cell dimensions were approximately (1×0.9×6) nm^3. Twin boundaries were generated with Atomsk[51] by imposing [11$\bar{2}$] and [$\bar{1}$10] orientations along the x and y directions, respectively, and [111] along the z direction. The separation between adjacent twins was 6-nm. Shear and tensile deformation were modeled following an approach closely aligned with that described in the reference[52].

To equilibrate the initial configurations before applying shear or tensile deformation, simulations were first run in the NPT ensemble using a Parrinello--Rahman barostat[53] and a Langevin thermostat at 300 K, allowing both the cell volume and shape to relax. This was followed by an NVT stage at 300 K controlled by a Nosé-Hoover thermostat. Equilibration was considered complete once the diagonal stress components satisfied $|\sigma_{ii}| \leq 0.9$ GPa ($i = x, y, z$) when averaged over the final 500 steps of the NVT run.

Shear deformation was introduced by incrementally tilting the simulation cell to impose a 2% strain in the ε_{zx} component. For uniaxial tensile, a 2% incremental strain was applied to the ε_{xx} component at each deformation step. After reaching the desired strain values, an additional 2 ps of NVT dynamics at 300 K was performed in the deformed cell using a Nosé-Hoover thermostat. Shear and tensile stresses were computed from the final 500 steps of these NVT simulations. Structural visualization and analysis were carried out using OVITO[54]. Radial distribution functions were obtained using the Coordination Analysis modifier with a cutoff of 5 Å, and bonding information was evaluated using the Bond Angel Distribution Analysis modifier with a cutoff distance of 3.2 Å.

Statistical analysis

All quantitative data are reported as mean ± standard deviation unless otherwise stated. Each data point represents the average value obtained from multiple independent measurements. Error bars in all Figures denote the standard deviation.

For Fig. S1d, the grain size distribution along the growth direction was analyzed at three selected positions: near the substrate ($n = 32$ individual grains), at the center ($n = 27$ individual grains), and near the surface ($n = 35$ individual grains). The resulting grain size distributions were fitted using a normal (Gaussian) distribution. In the corresponding box plots, the lower and upper boundaries of the rectangles represent the 25th and 75th percentiles, respectively.

Twin spacing statistics shown in Fig. S3 were obtained from high-resolution TEM images or dark-field TEM images by measuring the coherent twin boundary (CTB) spacing. The sample size was 238 for hnt-TaN and 124 for nt-TaN/TiN. The fitting curves in Fig. S3b were generated using kernel density estimation (KDE).

The grain size distribution histogram in Fig. S5 was derived from BF STEM images by measuring the sizes of 315 individual grains. The corresponding fitting curve follows a log-normal distribution.

The statistical distribution of misorientation angles between neighboring (001)-oriented grains in Fig. S6c was obtained from HRTEM images by analyzing 85 grain boundaries. Coincidence site lattice (CSL) boundaries were classified according to the following criteria: Σ5: 36.87° (34.87°–38.87°), Σ13: 22.62° (20.62°–24.62°), Σ17: 28.07° (26.07°–30.07°), Σ29: 43.60° (41.60°–45.60°), Σ37: 31.89° (29.89°–33.89°), Σ41: 38.68° (36.68°–40.68°).

For the micropillar compression tests shown in Fig. 2, $n = 7$ independent micropillars for nt-TaN/TiN and $n = 12$ independent micropillars for hnt-TaN were tested to ensure statistical reliability.

The statistical analyses presented in Fig. 4h and Fig. S13 were based on atomic position data extracted from identically sized regions in HRTEM images, containing 13 rows by 18 columns of atoms. The resulting distributions were fitted using a normal distribution.

Reporting summary

Further information on research design is available in the Nature Portfolio Reporting Summary linked to this article.

Data availability

All relevant data supporting the findings of this study are available within the paper and Supplementary Information. Source Data are provided with this paper. The datasets generated and/or analysed during the current study are available in the Figshare repository [https://figshare.com/] with the identifier https://doi.org/10.6084/m9.figshare.33207126.

References

1. Callister Jr, W. D. & Rethwisch, D. G. *Fundamentals of materials science and engineering: an integrated approach*. (John Wiley & Sons, 2020).
2. Musil, J. Hard and superhard nanocomposite coatings. *Surf. Coat. Technol.* **125**, 322–330 (2000).
3. Cain, M. & Morrell, R. Nanostructured ceramics: a review of their potential. *Appl. Organomet. Chem.* **15**, 321–330 (2001).
4. Li, J. et al. Nanoscale stacking fault–assisted room temperature plasticity in flash-sintered TiO2. *Sci. Adv.* **5**, eaaw5519 (2019).
5. Cho, J. et al. High temperature deformability of ductile flash-sintered ceramics via in-situ compression. *Nat. Commun.* **9**, 2063 https://doi.org/10.1038/s41467-018-04333-2 (2018).
6. Mishra, A. K. et al. Strategies for damage tolerance enhancement in metal/ceramic thin films: Lessons learned from Ti/TiN. *Acta Materialia* **228**, 117777 https://doi.org/10.1016/j.actamat.2022.117777 (2022).
7. Yang, W., Ayoub, G., Salehinia, I., Mansoor, B. & Zbib, H. Deformation mechanisms in Ti/TiN multilayer under compressive loading. *Acta Materialia* **122**, 99–108 https://doi.org/10.1016/j.actamat.2016.09.039 (2017).
8. Gao, J. et al. Facile route to bulk ultrafine-grain steels for high strength and ductility. *Nature* **590**, 262–267 https://doi.org/10.1038/s41586-021-03246-3 (2021).
9. Wei, Y. et al. Evading the strength–ductility trade-off dilemma in steel through gradient hierarchical nanotwins. *Nat. Commun.* **5**, 3580 https://doi.org/10.1038/ncomms4580 (2014).
10. Zhao, S. et al. Cryoforged nanotwinned titanium with ultrahigh strength and ductility. *Science* **373**, 1363–1368 https://doi.org/10.1126/science.abe7252 (2021).
11. Lai, A., Du, Z., Gan, C. L. & Schuh, C. A. Shape Memory and Superelastic Ceramics at Small Scales. *Science* **341**, 1505–1508 https://doi.org/10.1126/science.1239745 (2013).
12. GARVIE, R., HANNINK, R. & PASCOE, R. Ceramic steel? *Nature* **258**, 703–704 (1975).
13. Swain, M. Shape memory behaviour in partially stabilized zirconia ceramics. *Nature* **322**, 234–236 (1986).

14. Zhang, J. et al. Plastic deformation in silicon nitride ceramics via bond switching at coherent interfaces. *Science* **378**, 371–376 https://doi.org/10.1126/science.abq7490 (2022).
15. Sangiovanni, D. G. et al. Controlled polymorphic competition – A path to tough and hard ceramics. *Acta Materialia* **294**, 121121 https://doi.org/10.1016/j.actamat.2025.121121 (2025).
16. Lin, S. et al. Shear-activated phase transformations of diborides via machine-learning potential molecular dynamics. *Acta Materialia* **301**, 121606 https://doi.org/10.1016/j.actamat.2025.121606 (2025).
17. Bu, Y. et al. Activating deformation twinning in cubic boron nitride. *Nat. Mater.* **24**, 361–368 https://doi.org/10.1038/s41563-024-02111-8 (2025).
18. Yan, G.-Q., Cheng, X.-L. & Zhang, H. Phase stability and mechanical response of tantalum nitrides to electronic excitation effect. *Mater. Res. Express* **7**, 066508 https://doi.org/10.1088/2053-1591/ab95d5 (2020).
19. Koutná, N. et al. Point-defect engineering of MoN/TaN superlattice films: A first-principles and experimental study. *Mater. Des.* **186**, 108211 https://doi.org/10.1016/j.matdes.2019.108211 (2020).
20. Rydén, G. Ab initio *lattice dynamics and Anharmonic effects in refractory Rock-salt structure TaN ceramic*. Master Thesis, Linköping University, Sweden (2020) thesis, (2020).
21. Huang, Y. et al. Harvesting superior intrinsic plasticity in nitride ceramics with negative stacking fault energy. *Acta Materialia* **286**, 120774 https://doi.org/10.1016/j.actamat.2025.120774 (2025).
22. Huang, Y. et al. Highly nanotwinned transition metal nitride film enabled by negative stacking fault energy. *Acta Materialia* **299**, 121475 https://doi.org/10.1016/j.actamat.2025.121475 (2025).
23. Frisk, K. Analysis of the phase diagram and thermochemistry in the Ta–N and the Ta–C–N systems. *J. Alloy. Compd.* **278**, 216–226 (1998).
24. Lee, H. et al. High-pressure synthesis and thermal conductivity of semimetallic θ-tantalum nitride. *Adv. Funct. Mater.* **33**, 2212957 (2023).
25. Koutná, N., Holec, D., Svoboda, O., Klimashin, F. & Mayrhofer, P. First-principles study on the energetic properties of point defects in cubic Mo-N and Ta-N. https://doi.org/10.48550/arXiv.1604.02718 (2016).
26. Klimashin, F. F., Lobmaier, L., Koutná, N., Holec, D. & Mayrhofer, P. H. The MoN–TaN system: Role of vacancies in phase stability and mechanical properties. *Mater. Des.* **202**, 109568 https://doi.org/10.1016/j.matdes.2021.109568 (2021).
27. Bhattacharyya, D., Mara, N. A., Dickerson, P., Hoagland, R. G. & Misra, A. Compressive flow behavior of Al–TiN multilayers at nanometer scale layer thickness. *Acta Materialia* **59**, 3804–3816 https://doi.org/10.1016/j.actamat.2011.02.036 (2011).
28. Shin, C., Jin, H.-H., Kim, W.-J. & Park, J.-Y. Mechanical Properties and Deformation of Cubic Silicon Carbide Micropillars in Compression at Room Temperature. *J. Am. Ceram. Soc.* **95**, 2944–2950 https://doi.org/10.1111/j.1551-2916.2012.05346.x (2012).
29. Liu, S., Wheeler, J. M., Michler, J., Zeng, X. T. & Clegg, W. J. Plastic flow at the theoretical yield stress in ceramic films. *Scr. Materialia* **117**, 24–27 https://doi.org/10.1016/j.scriptamat.2016.02.008 (2016).
30. Mayer, C. R. et al. Anisotropy, size, and aspect ratio effects on micropillar compression of AlSiC nanolaminate composites. *Acta Materialia* **114**, 25–32 https://doi.org/10.1016/j.actamat.2016.05.018 (2016).
31. Csanádi, T., Castle, E., Reece, M. J. & Dusza, J. Strength enhancement and slip behaviour of high-entropy carbide grains during micro-compression. *Sci. Rep.* **9**, 10200 https://doi.org/10.1038/s41598-019-46614-w (2019).
32. Ramachandramoorthy, R. et al. Dynamic Plasticity and Failure of Microscale Glass: Rate-Dependent Ductile–Brittle–Ductile Transition. *Nano Lett.* **19**, 2350–2359 https://doi.org/10.1021/acs.nanolett.8b05024 (2019).
33. Pshyk, A. V. et al. High-entropy transition metal nitride thin films alloyed with Al: Microstructure, phase composition and mechanical properties. *Mater. Des.* **219**, 110798 https://doi.org/10.1016/j.matdes.2022.110798 (2022).
34. Frankberg, E. J. et al. Exceptional Microscale Plasticity in Amorphous Aluminum Oxide at Room Temperature. *Adv. Mater.* **35**, 2303142 https://doi.org/10.1002/adma.202303142 (2023).
35. Shen, C. et al. Achieving room temperature plasticity in brittle ceramics through elevated temperature preloading. *Sci. Adv.* **10**, eadj4079 https://doi.org/10.1126/sciadv.adj4079 (2024).
36. Liu, L. et al. Nanotwinned CrN ceramics with enhanced plasticity. *Nat. Commun.* **16**, 5934 https://doi.org/10.1038/s41467-025-61275-2 (2025).
37. Zhang, J. et al. Scale-bridging dislocation plasticity in MgO at room temperature. *Int. J. Plasticity* **195**, 104533 https://doi.org/10.1016/j.ijplas.2025.104533 (2025).
38. Sebastiani, M., Johanns, K. E., Herbert, E. G. & Pharr, G. M. Measurement of fracture toughness by nanoindentation methods: Recent advances and future challenges. *Curr. Opin. Solid State Mater. Sci.* **19**, 324–333 https://doi.org/10.1016/j.cossms.2015.04.003 (2015).
39. Larsson, P.-L. & Giannakopoulos, A. E. Tensile stresses and their implication to cracking at pyramid indentation of pressure-sensitive hard metals and ceramics. *Mater. Sci. Eng.: A* **254**, 268–281 https://doi.org/10.1016/S0921-5093(98)00752-7 (1998).
40. Sangiovanni, D. G., Kaufmann, K. & Vecchio, K. Valence electron concentration as key parameter to control the fracture resistance of refractory high-entropy carbides. *Sci. Adv.* **9**, eadi2960 https://doi.org/10.1126/sciadv.adi2960 (2023).
41. Lorentzon, M. et al. Metal-like ductility and high hardness in nitrogen-rich HfN thin films by point defect superstructuring. *Commun. Mater.* **6**, 46 https://doi.org/10.1038/s43246-025-00768-5 (2025).
42. Jain, A. et al. Commentary: The Materials Project: A materials genome approach to accelerating materials innovation. *APL materials* **1** https://doi.org/10.1063/1.4812323 (2013).
43. Oliver, W. C. & Pharr, G. M. An improved technique for determining hardness and elastic modulus using load and displacement sensing indentation experiments. *J. Mater. Res.* **7**, 1564–1583 https://doi.org/10.1557/JMR.1992.1564 (1992).
44. Zhang, Q., Zhang, L., Jin, C., Wang, Y. & Lin, F. CalAtom: A software for quantitatively analysing atomic columns in a transmission electron microscope image. *Ultramicroscopy* **202**, 114–120 (2019).
45. Nord, M., Vullum, P. E., MacLaren, I., Tybell, T. & Holmestad, R. Atomap: a new software tool for the automated analysis of atomic resolution images using two-dimensional Gaussian fitting. *Adv. Struct. Chem. Imaging* **3**, 9 https://doi.org/10.1186/s40679-017-0042-5 (2017).
46. Wheeler, J. M., Niederberger, C., Tessarek, C., Christiansen, S. & Michler, J. Extraction of plasticity parameters of GaN with high temperature, in situ micro-compression. *Int. J. Plasticity* **40**, 140–151 https://doi.org/10.1016/j.ijplas.2012.08.001 (2013).
47. Sneddon, I. N. The relation between load and penetration in the axisymmetric Boussinesq problem for a punch of arbitrary profile. *Int. J. Eng. Sci.* **3**, 47–57 (1965).
48. Kresse, G. & Furthmüller, J. Efficient iterative schemes for ab initio total-energy calculations using a plane-wave basis set. *Phys. Rev. B* **54**, 11169 (1996).
49. Kresse, G. & Joubert, D. From ultrasoft pseudopotentials to the projector augmented-wave method. *Phys. Rev. b* **59**, 1758 (1999).
50. Perdew, J. P., Burke, K. & Ernzerhof, M. Generalized gradient approximation made simple. *Phys. Rev. Lett.* **77**, 3865 (1996).

51. Hirel, P. Atomsk: A tool for manipulating and converting atomic data files. *Computer Phys. Commun.* **197**, 212–219 (2015).
52. Koutná, N. et al. Atomistic mechanisms underlying plasticity and crack growth in ceramics: a case study of AlN/TiN superlattices. *Acta Materialia* **229**, 117809 (2022).
53. Parrinello, M. & Rahman, A. Polymorphic transitions in single crystals: A new molecular dynamics method. *J. Appl. Phys.* **52**, 7182–7190 (1981).
54. Stukowski, A. Visualization and analysis of atomistic simulation data with OVITO–the Open Visualization Tool. *Model. Simul. Mater. Sci. Eng.* **18**, 015012 (2009).
55. Zeilinger, A. et al. Mechanical property enhancement in laminates through control of morphology and crystal orientation. *J. Phys. D: Appl. Phys.* **48**, 295303 https://doi.org/10.1088/0022-3727/48/29/295303 (2015).
56. Hahn, R. et al. Superlattice effect for enhanced fracture toughness of hard coatings. *Scr. Materialia* **124**, 67–70 https://doi.org/10.1016/j.scriptamat.2016.06.030 (2016).
57. Meindlhumer, M. et al. Precipitation-based grain boundary design alters Inter- to Trans-granular Fracture in AlCrN Thin Films. *Acta Materialia* **237**, 118156 https://doi.org/10.1016/j.actamat.2022.118156 (2022).
58. Buchinger, J. et al. Fracture toughness trends of modulus-matched TiN/(Cr, Al) N thin film superlattices. *Acta Materialia* **202**, 376–386 (2021).
59. Kainz, C., Pohler, M., Tkadletz, M., Czettl, C. & Schalk, N. The influence of bias voltage on structure, thermal stability and mechanical properties of arc evaporated Cr0. 69Ta0. 20B0. 11N coatings. *Surf. Coat. Technol.* **428**, 127867 (2021).
60. Hahn, R. et al. Mechanistic study of superlattice-enabled high toughness and hardness in MoN/TaN coatings. *Commun. Mater.* **1**, 62 https://doi.org/10.1038/s43246-020-00064-4 (2020).
61. Buchinger, J. et al. Toughness enhancement in TiN/WN superlattice thin films. *Acta Materialia* **172**, 18–29 (2019).
62. Drnovšek, A. et al. High temperature fracture toughness of single-layer CrAlN and CrAlSiN hard coatings. *Surf. Coat. Technol.* **409**, 126909 (2021).
63. Bartosik, M. et al. Fracture toughness of Ti-Si-N thin films. *Int. J. Refractory Met. Hard Mater.* **72**, 78–82 (2018).
64. Bartosik, M., Rumeau, C., Hahn, R., Zhang, Z. & Mayrhofer, P. Fracture toughness and structural evolution in the TiAlN system upon annealing. *Sci. Rep.* **7**, 16476 (2017).
65. Gao, Z. et al. Ab initio supported development of TiN/MoN superlattice thin films with improved hardness and toughness. *Acta Materialia* **231**, 117871 https://doi.org/10.1016/j.actamat.2022.117871 (2022).
66. Bermanschläger, S. C. et al. Structure, chemistry, and mechanical properties of non-reactively sputtered Ti-Al-N. *Mater. Des.* **252**, 113803 https://doi.org/10.1016/j.matdes.2025.113803 (2025).
67. Zhang, J. et al. Effect of asymmetric interfaces on the spinodal decomposition of (Ti,Al)N/ZrN multilayers: First-principles and experimental investigations. *J. Alloy. Compd.* **1003**, 175558 https://doi.org/10.1016/j.jallcom.2024.175558 (2024).
68. Gao, Z. et al. Bilayer period and ratio dependent structure and mechanical properties of TiN/MoN superlattices. *Acta Materialia* **279**, 120313 https://doi.org/10.1016/j.actamat.2024.120313 (2024).
69. Chen, L. et al. Microstructure and mechanical properties of (AlCrTiZrV)Nx high-entropy alloy nitride films by reactive magnetron sputtering. *Vacuum* **181**, 109706 https://doi.org/10.1016/j.vacuum.2020.109706 (2020).
70. Kretschmer, A., Rojacz, H., Badisch, E., Polcik, P. & Mayrhofer, P. H. High-temperature tribological behavior of high-entropy sublattice oxide, nitride, and diboride coatings. *Surf. Coat. Technol.* **489**, 131037 https://doi.org/10.1016/j.surfcoat.2024.131037 (2024).
71. Janknecht, R. et al. A Strategy to Enhance the B-Solubility and Mechanical Properties of Ti–B–N Thin Films. *Acta Materialia* **271**, 119858 https://doi.org/10.1016/j.actamat.2024.119858 (2024).
72. Zauner, L. et al. Assessing the fracture and fatigue resistance of nanostructured thin films. *Acta Materialia* **239**, 118260 https://doi.org/10.1016/j.actamat.2022.118260 (2022).
73. Zhang, Y., Bartosik, M., Brinckmann, S., Lee, S. & Kirchlechner, C. Toughening nitride hard coatings by deflecting cracks along grain boundaries. *Mater. Sci. Eng.: A* **935**, 148392 https://doi.org/10.1016/j.msea.2025.148392 (2025).
74. Shin, C.-S. et al. Epitaxial growth of metastable δ-TaN layers on MgO (001) using low-energy, high-flux ion irradiation during ultrahigh vacuum reactive magnetron sputtering. *J. Vac. Sci. Technol. A: Vac., Surf., Films* **20**, 2007–2017 (2002).

Acknowledgements

The authors would like to thank Velislava Terziyska (Montanuniversität Leoben) for the film deposition. We also thank Zequn Zhang, Xiaoming Liu, and Qiulin Qu from the Erich Schmid Institute of Materials Science for their valuable assistance with the experimental work. We acknowledge CzechNanoLab Research Infrastructure supported by the MEYS CR (LM2023051) .

Author contributions

Y.H. designed the experiments, performed experiments, analyzed the data, and wrote the manuscript with input from all authors. Z.C. helped analyze the data and discussed the results. K.R. and N.K performed AIMD simulations and analysis. R.H. conducted micropillar compression and analysis. V.M.K. performed the nanoindentation experiments and analysis. J.K. conducted pole Fig. measurements and analysis. C.M. provided suggestions on the film synthesis. Z. L. Z. conceived the idea, directed the research, and discussed the results. All co-authors participated in the manuscript revision.

Funding

The financial support (Y.H., Z.C., and Z.L.Z.) by the Austrian Science Fund (10.55776/PAT1946623) is highly acknowledged.

Competing interests

The authors declare no competing interests.

Declaration of AI

Gemini and DeepSeek were used solely to improve the clarity and grammar of the manuscript. All suggestions were reviewed and edited by the authors, who take full responsibility for the content of the manuscript.

Additional information

Supplementary information The online version contains supplementary material available at https://doi.org/10.1038/s41467-026-79377-w.

Correspondence and requests for materials should be addressed to Zaoli Zhang.

Peer review information *Nature Communications* thanks Davide Sangiovanni and Zhongzhen Wu for their contribution to the peer review of this work. A peer review file is available.

Reprints and permissions information is available at http://www.nature.com/reprints

Publisher's note Springer Nature remains neutral with regard to jurisdictional claims in published maps and institutional affiliations.

Open Access This article is licensed under a Creative Commons Attribution 4.0 International License, which permits use, sharing, adaptation, distribution and reproduction in any medium or format, as long as you give appropriate credit to the original author(s) and the source, provide a link to the Creative Commons licence, and indicate if changes were made. The images or other third party material in this article are included in the article's Creative Commons licence, unless indicated otherwise in a credit line to the material. If material is not included in the article's Creative Commons licence and your intended use is not permitted by statutory regulation or exceeds the permitted use, you will need to obtain permission directly from the copyright holder. To view a copy of this licence, visit http://creativecommons.org/licenses/by/4.0/.

© The Author(s) 2026

This Article in Press is shared early to give you faster access to new research. It is citable and carries a permanent DOI. The final edited version will replace it automatically.